Breakthrough Study of CO_2 Adsorption and Regeneration Performance of Mn- and Ce-Doped Ni–Al Layered Double Hydroxides Derived Mixed Oxides in Packed-Bed Column

Ararso N. Wagassa, Enyew A. Zereffa,* Tofik A. Shifa,* and Amit Bansiwal*

Carbon dioxide (CO_2) capture is an important strategy to mitigate greenhouse gas emissions and reduce global warming effects. This study synthesizes two nanomaterials, Ce-doped Ni–Al mixed metal oxide (CNAO) and Mn-doped Ni–Al mixed metal oxide (MNAO), from Mn- and Ce-doped Ni–Al-layered double hydroxides using a co-precipitation method followed by a calcination process. The materials are characterized using various techniques, such as High-resolution transmission electron microscopy-energy dispersive x-ray spectroscopy/selected area electron dispersion (HRTEM-EDS/SAED), X-ray diffraction (XRD), x-ray photoelectron spectroscopy (XPS), Brunauer-Emmett-Teller (BET), and attenuated total reflection Fourier transform infrared (ATR FT-IR). The CO_2 adsorption performance of the materials is evaluated using packed-bed column experiments at the testing conditions of 13 vol% $\pm$ 1 vol% CO_2 in N_2 simulated flue gas, flow rate of 20 mL min^{-1}, inlet pressure of 14.15 $\pm$ 0.1 psi, and temperature of 31 °C $\pm$ 2 °C. The results show that both CNAO and MNAO are promising nanomaterials for CO_2 capture applications due to their high CO_2 adsorption capacity and efficiency. CNAO has a higher saturation capacity of 11.4 mmol g^{-1} and a longer breakthrough time than MNAO, which has a saturation capacity of 10.0 mmol g^{-1}. The doping of Ce and Mn enhances the CO_2 adsorption capacity of the materials compared to the un-doped Ni–Al mixed oxide. The mechanisms of CO_2 adsorption are mainly linearly adsorbed CO_2, bidentate, and monodentate or bulk carbonate formation, as revealed by ATR FT-IR analysis. The regeneration performance results suggest that CNAO is more stable than MNAO under multiple regeneration cycles and more promising material for large-scale CO_2 capture applications.

1. Introduction

Climate change is a widely recognized modern threat throughout the world. CO_2, a greenhouse gas, is a major contributor to global warming and climate change. Therefore, developing efficient and sustainable methods for CO_2 capture and utilization is of great importance. Scientists and researchers have been continually looking for innovative ways to mitigate greenhouse gas emissions. Among the various methods, adsorption is considered a promising technique because of its low energy consumption, high selectivity, and easy operation.[1,2] However, conventional adsorbents, including activated carbon, zeolites, and metal–organic frameworks, have some drawbacks, such as low CO_2 adsorption capacity, high regeneration cost, and poor stability.[3]

Layered double hydroxides (LDHs) are a class of materials that have shown potential for CO_2 adsorption due to their tunable structure, composition, and surface properties. LDHs are made up of positively charged metal hydroxide layers alternating with layers of interlayer anions. These interlayer anions can be exchanged with CO_2 molecules.[4] LDHs can also be calcined to form mixed metal oxides (MMOs) that have higher surface area and basicity than LDHs.[5,6] However, there are still some challenges and gaps that need to be addressed for LDHs and MMOs to be applied for CO_2 adsorption. One of these gaps is the effect of the metal cations, the interlayer anions, and the calcination temperature on the CO_2 adsorption performance of LDHs and MMOs. The other gap is the stability and recyclability of LDHs and MMOs under different conditions, such as humidity, temperature, and CO_2 concentration.[7,8]

A. N. Wagassa, A. Bansiwal
Environmental Sustainability and Green Economy
CSIR-National Environmental Engineering Institute
Nehru Marg, Nagpur 440020, India
E-mail: ak_bansiwal@neeri.res.in

A. N. Wagassa, E. A. Zereffa
Department of Applied Chemistry
Adama Science and Technology University
P.O. Box 1888, Adama Ethiopia
E-mail: eneyew.amare@astu.edu.et

T. A. Shifa
Department of Molecular Science and Nanosystem
Ca' Foscari University of Venice
Via Torino 155, Venezia, Mestre 30172, Italy
E-mail: tofikahmed.shifa@unive.it

**ADVANCED
SCIENCE NEWS**

www.advancedsciencenews.com

**ADVANCED
SUSTAINABLE
SYSTEMS**

www.advsustainsys.com

The rise of chemisorbent materials for CO_2 capture lies in their impressive capacity to adsorb large amounts and release the gas readily. Within this category, double oxides, hydrotalcite compounds, and their calcined derivatives have emerged as promising candidates. Extensive reviews have compared these materials, delving into their general properties and remarkable adsorption capacities. Notably, hydrotalcites have garnered interest as intermediate-temperature chemisorbents.[9,10] A recent study by Garcés-Polo et al. has shown that Ni-based mixed oxides, calcined $Mg_{3−x}Ni_xAl–CO_3$, exhibited significantly higher sorption capacity than other hydrotalcite-based materials under comparable conditions.[9] The sorption capacities of Ni-based mixed oxides derived from hydrotalcite can be further improved through doping with other metal cations such as Manganese (Mn) and Cerium (Ce). Ce and Mn have multiple oxidation states, enabling them to participate in redox cycles during adsorption. This enhances the efficiency and selectivity of the adsorption process. Ce and Mn can also facilitate the activation and transfer of oxygen molecules on the adsorbent surface, leading to faster reaction rates. This is particularly beneficial for oxidation reactions. Further, these cations can also create electron-deficient sites on the surface of the adsorbent which can act like magnets for CO_2 molecules, further boosting the adsorption capacity.[11]

One of the approaches to evaluate the CO_2 adsorption performance of LDHs and MMOs is to use packed-bed column systems that closely resemble the practical application in the field. A packed-bed column is a device that consists of a cylindrical tube filled with adsorbent particles. CO_2 gas mixture flows through the column and contacts with the adsorbent particles. The breakthrough curve is obtained by measuring the outlet CO_2 concentration as a function of time. It can provide information about the adsorption capacity, selectivity, mass transfer, and kinetics of the adsorbent. However, there are still some gaps that need to be filled for using a packed-bed column system to study CO_2 adsorption on LDHs and MMOs. The effect of the particle size, shape, and distribution of LDHs and MMOs plays a major role in the performance of a packed-bed column. The column diameter, length, and configuration also affect the pressure drop, heat transfer, and mass transfer in the column. In addition, the flow rate, temperature, pressure, and composition of the gas mixture influence the breakthrough curve.[12–14]

Mixed metal oxides have been extensively synthesized, characterized, and evaluated for CO_2 capture performance.[8,15,16] Packed-bed reactors are, in reality, a well-established technique for evaluating the CO_2 adsorption performance of MMOs, with a significant body of research dedicated to this area. Recent review articles, such as those by Garcés-Polo et al.[9] and Li et al.,[10] provide insightful summaries of MMOs as high-temperature CO_2 adsorbents and their successful implementation in packed-bed configurations.[17] While acknowledging the value of alternative evaluation methods, packed-bed reactors remain a cornerstone for developing efficient and scalable MMO-based CO_2 capture systems. By addressing emerging trends and challenges in this area, we can further accelerate the development of these promising materials for mitigating climate change.

Therefore, this study is aimed to assess the CO_2 adsorption performance of Mn- and Ce-doped Ni–Al mixed metal oxides in a packed-bed column system. The MMOs are obtained from Mn-doped as well as Ce-doped Ni–Al layered double hydroxides by calcination at high temperature. The LDHs are made up of positively charged Ni–Al hydroxide layers in which Ce^{4+} and Mn^{2+} are supposed to replace Al and Ni, respectively, by 5% in the layers and negatively charged $CO_3^{2−}$ interlayers. Both Ce and Mn doping can boost the CO_2 adsorption capacity of Ni–Al MMOs by increasing the basicity, surface, and redox properties of the material. This research contributes to the development of more efficient and economical CO_2 capture technologies by reducing environmental damage. The CO_2 adsorption performance of the MMOs was evaluated using fixed-bed column experiments with upward flow of simulated flue gas (13 vol% ±1 vol% CO_2 in N_2) at a flow rate of 20 L min$^{−1}$. The inlet pressure was maintained at 14.15 ± 0.1 psi, reflecting typical flue gas pressure in industrial settings. The temperature was controlled within 31 °C ± 2 °C to account for potential temperature fluctuations during operation.
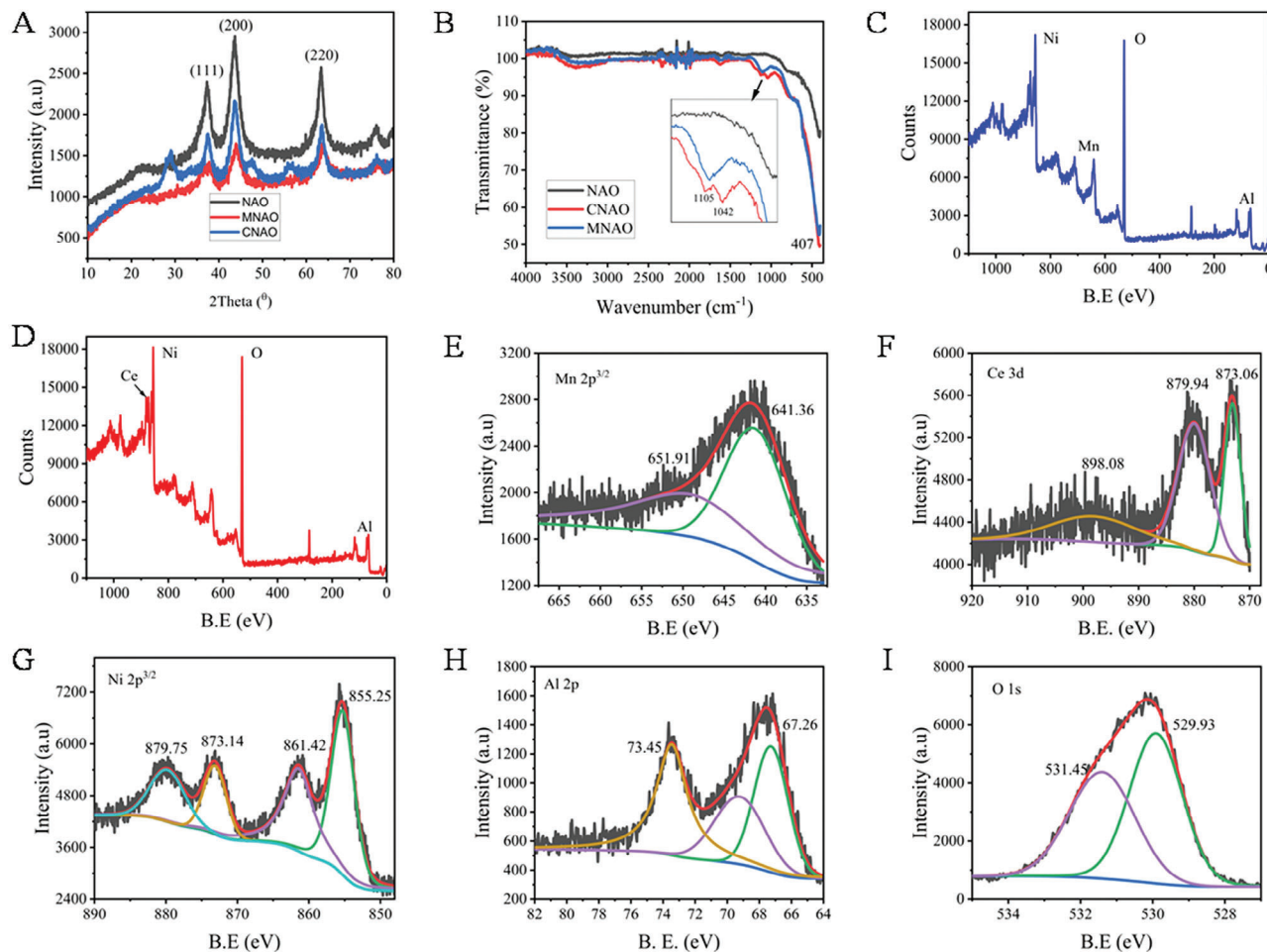
2. Results and Discussion

2.1. CNAO and MNAO Characterizations

The crystal structures of CNAO and MNAO were determined using X-ray diffraction (XRD) analysis. The XRD patterns of these materials showed sharp peaks that corresponded to the cubic structure with the space group Fm-3m (**Figure 1A**).[18,19] The lattice parameters of CNAO and MNAO were calculated from the XRD data by using the Bragg Equation - Equation (S1), Supporting Information, and were found to be 4.14 Å for both mixed metal oxides (Table S1, Supporting Information,). The average crystallite sizes of CNAO and MNAO were assessed using the Debye–Scherrer Equation (1):[20]

$$D = \frac{K\lambda}{\beta \cos\theta} \tag{1}$$

where D is the average crystallite size, K is a shape factor (usually 0.9), λ is the wavelength of the XRD (1.5406 Å for Cu Kα), β is the full width at half maximum of the peak, and θ is the Bragg angle. The average crystallite sizes of CNAO and MNAO were found to be 3.32 and 3.68 nm, respectively (Table S1, Supporting Information). The influence of Mn and Ce doping on the crystallinity and peak intensity of NAO was observed from these XRD results. The peak intensity was more diminished in Mn-doped NAO; while, no visible widening of the peaks was observed after doping in both cases. The appearance of new peaks was observed in Ce-doped NAO. This suggests that Mn doping leads to a decrease in the crystallinity of NAO; while, Ce doping may lead to the formation of new crystal phases.

The nature of the bonds and elemental compositions of CNAO and MNAO were confirmed by attenuated total reflection Fourier transform infrared (ATR FT-IR) and x-ray photoelectron spectroscopy (XPS) analyses, respectively. The ATR FT-IR spectra of both materials showed distinct peaks that indicated the presence of metal—oxygen bonds (Figure 1B). CNAO displayed a peak at 1042 cm$^{−1}$, which was ascribed to the Ce—O bond.[21] At the same time, MNAO exhibited a peak at 1105 cm$^{−1}$, which was attributed to the Mn—O bond.[22] The elemental survey from XPS spectra reveals the presence of all the expected elements; namely Ni, Al, O, and Mn in MNAO (Figure 1C) and Ni, Al, O, and Ce in CNAO

**ADVANCED
SCIENCE NEWS**

www.advancedsciencenews.com

**ADVANCED
SUSTAINABLE
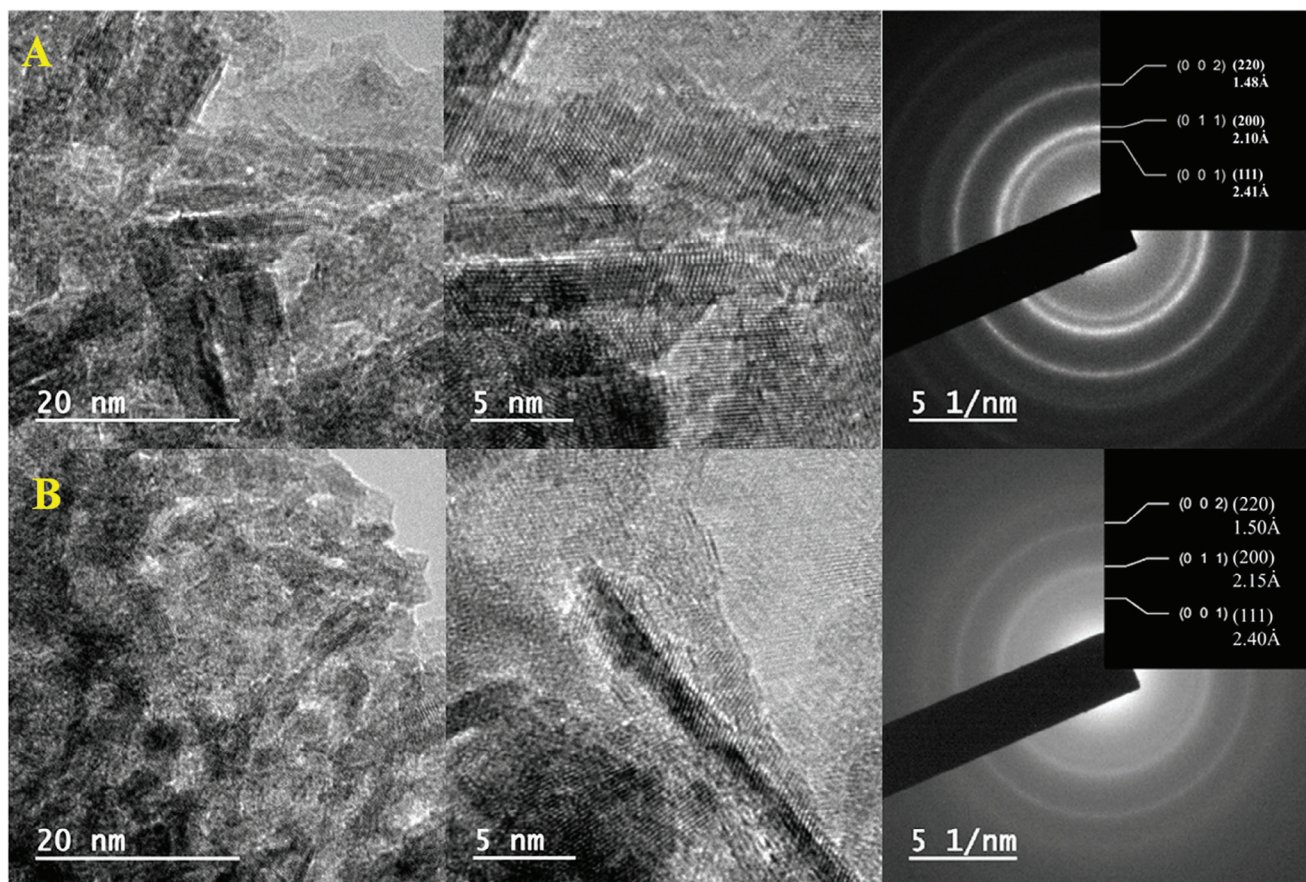SYSTEMS**

www.advsustainsys.com

Figure 1. A) XRD, B) ATR FT-IR, and C–I) XPS spectra of MNAO containing 5% Mn and CNAO containing 5% Ce.

(Figure 1D). Further XPS analysis provided powerful information regarding the oxidation states of Ce and Mn in CNAO and MNAO, respectively. The Ce 3d spectrum of CNAO showed two doublets at 873.07 eV for Ce 3d5/2 and at 879.95 eV and 898.36 eV for Ce 3d3/2, which indicated the presence of Ce^{4+} (Figure 1F).[23] Similarly, the Mn 2p spectrum of MNAO showed two doublets at 641.17 eV for Mn 2p3/2 and at 649.11 eV for Mn 2p1/2, which suggested the presence of Mn^{2+} (Figure 1E).[24,25]

The EDS analysis of the TEM images confirmed the successful incorporation of Mn and Ce into the Ni–Al LDH structure, as shown by the presence of these elements in MNAO and CNAO, respectively, along with Ni, Al, and O (Figure S1A,B, Supporting Information). The mole ratios of divalent to trivalent cations in both samples were close to the ideal value of 3:1, indicating a high degree of cation incorporation and a well-balanced charge in the layers. The mole ratio of Ni to (Al + Ce) was 2.6 in CNAO, and the mole ratio of (Ni + Mn) to Al was 2.5 in MNAO. The absence of C in both samples was consistent with the XPS results, which suggested the complete removal of the carbonate anions from the interlayer space during the calcination process. These results demonstrated the successful synthesis of Mn-doped and Ce-doped Ni–Al MOs by the co-precipitation method.

The morphology of CNAO and MNAO was examined by HRTEM analysis. The HRTEM images of both mixed oxides showed a sheet-like morphology with smooth edges and uniform thickness. The average sizes of CNAO and MNAO sheets were measured to be 3.17 and 4.28 nm, respectively (**Figure 2**). The HRTEM images also showed clear lattice fringes that indicated the crystalline nature of both materials. SAED patterns of CNAO and MNAO showed concentric rings that corresponded to the cubic structure with the space group Fm-3m as they were dominated by Ni and Al, which had a face-centered cubic (FCC) structure.[26] The d-spacing values obtained from High-resolution transmission electron microscopy-energy dispersive x-ray spectroscopy/selected area electron dispersion (HRTEM-SAED) analysis were found to align with those obtained from XRD analysis, further supporting the crystal structure determination.

The specific surface area (SSA) and porosity of CNAO and MNAO were determined by the Brunauer-Emmett-Teller (BET) method with N_2 adsorption–desorption isotherms. The BET SSAs of CNAO and MNAO were calculated to be 173.54 and 170.22 m^2 g^{-1}, respectively (Table S2, Supporting Information). The Barrett–Joyner–Halenda (BJH) model was applied to the des-

**ADVANCED
SCIENCE NEWS**

www.advancedsciencenews.com

**ADVANCED
SUSTAINABLE
SYSTEMS**

www.advsustainsys.com

Figure 2. A) HRTEM images and SAED pattern of MNAO (5% Mn) and B) HRTEM images and SAED pattern of CNAO (5% Ce).

orption branch of the isotherms to determine the pore size distribution of each mixed metal oxide. The pore size distribution curves showed that both CNAO and MNAO had mesoporous structures with pore diameters of 2.14–2.15 nm, respectively.
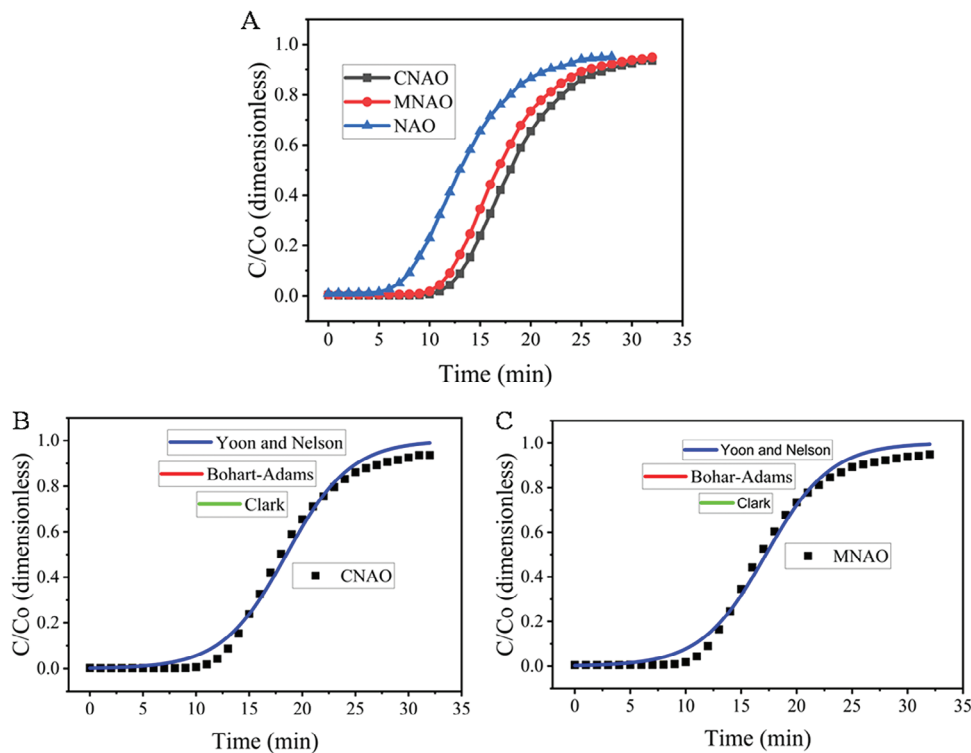
In summary, we synthesized CNAO and MNAO by using a simple co-precipitation method followed by calcination and characterized their crystal structure, elemental composition, and morphology using XRD, ATR FT-IR, XPS, and HRTEM-SAED analyses. We also measured their surface area and porosity using the Brunauer-Emmett-Teller (BET} method. The results showed that both mixed oxides had a cubic structure with the space group Fm-3m, a sheet-like morphology with nanoscale thickness, and a mesoporous structure with high surface area. The results also confirmed the presence of Ce^{4+} in CNAO and Mn^{2+} in MNAO in addition to Ni, Al, and O. These properties make CNAO and MNAO promising candidates for various applications such as adsorption, catalysis, energy storage, and sensing.

2.2. CO_2 Adsorption Performance and Breakthrough Curve of CNAO and MNAO

The breakthrough curve is employed to compare the CO_2 adsorption capacities of CNAO and MNAO, which are doped with Ce^{4+} and Mn^{2+}, respectively. The breakthrough curve plots the outlet CO_2 concentration versus time, as measured by the experimental setup shown in Figure 6. **Figure 3A** shows that CNAO has a higher adsorption capacity than MNAO as it takes longer to reach the breakthrough point. The breakthrough point is when the outlet percentage reaches 10% of the inlet percentage (13%). For CNAO, this occurs at ≈13 min; while, for MNAO, it occurs at ≈12 min. After the breakthrough point, the outlet concentration keeps increasing until it reaches a maximum value of 90% of the inlet at 28 min for CNAO and 26 min for MNAO. This is the saturation point, which indicates that the adsorbent is almost fully saturated. The service time, which is the difference between the saturation time and the breakthrough time, reflects the duration of effective adsorption.

The data in **Table 1** further supports this observation. The adsorption performance of CNAO is higher than that of MNAO, as indicated by the values of breakthrough capacity (q_b), saturation capacity (q_s), and equilibrium capacity (q_e). q_b (mmol g^{-1}) represents the amount of CO_2 adsorbed by the adsorbent at the beginning of the breakthrough. CNAO has a higher q_b value of 7.52 mmol g^{-1} relative to MNAO's value of 6.49 mmol g^{-1}, showing that CNAO can adsorb a larger quantity of CO_2 initially. q_s (mmol g^{-1}) represents the maximum amount of CO_2 that can be adsorbed by the adsorbent. CNAO has a higher q_s value of 11.16 mmol g^{-1} compared to MNAO's value of 9.81 mmol g^{-1}, demonstrating that CNAO has a higher overall CO_2 adsorption performance. q_e (mmol g^{-1}) represents the amount of CO_2 adsorbed by the adsorbent at equilibrium. CNAO again outper-

**ADVANCED
SCIENCE NEWS**

www.advancedsciencenews.com

**ADVANCED
SUSTAINABLE
SYSTEMS**

www.advsustainsys.com

Figure 3. A) Breakthrough curves of CO_2 adsorption on NAO (un-doped), CNAO (5% Ce), and MNAO (5% Mn) at 20 mL min^{-1} flow rate of CO_2, 31 °C, 14.15 psi, and 10 cm packed-bed height and B,C) fitted fixed-bed models.

Table 1. CO_2 adsorption efficiencies of CNAO (5% Ce) and MNAO (5% Mn).

Adsorbents	q_b [mmol g^{-1}]	q_s [mmol g^{-1}]	q_e [mmol g^{-1}]	Column efficiency [%]
CNAO	7.52	11.16	11.4	67.38
MNAO	6.49	9.81	10.0	66.16

forms MNAO in terms of CO_2 adsorption performance, with a q_e value of 11.4 mmol g^{-1} relative to MNAO's value of 10.0 mmol g^{-1}.

Therefore, the data indicates that CNAO, with Ce^{4+} dopant, exhibits better CO_2 adsorption performance than MNAO, with Mn^{2+} dopant. Further, CNAO has a longer breakthrough time, suggesting its potential for effective CO_2 capture applications. As a result, it can be concluded that CNAO is a better adsorbent than MNAO for CO_2 capture from flue gas streams.

In addition to the most common contributing factors such as surface entrapments and metal–CO_2 interactions, oxygen vacancies and redox pairs (Ce^{4+}/Ce^{3+} and Mn^{2+}/Mn^{3+}) are likely key contributors to the enhanced CO_2 capture by Ce- and Mn-doped Ni–Al MOs where oxygen vacancies act as adsorption sites; while, redox pairs facilitate CO_2 binding.[27–29]
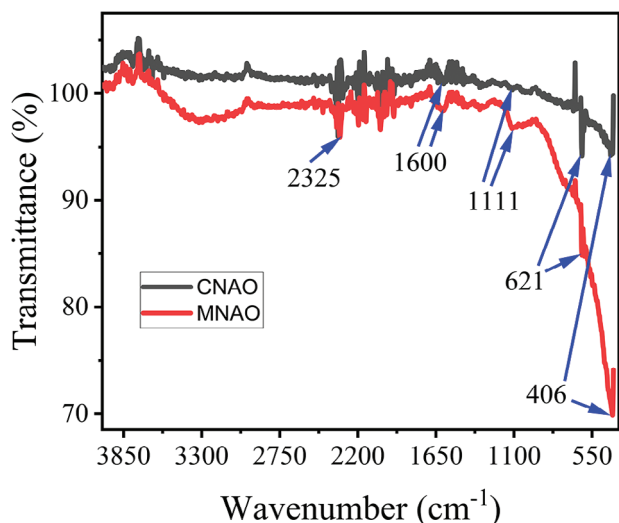
2.3. Studying the Breakthrough Curves Fitting With Fixed-Bed Models

CO_2 adsorption capacity and selectivity of Ni–Al mixed oxide doped with Ce or Mn were investigated in this study. The break-

Table 2. Fixed-bed models fitted with the CO_2 adsorbed onto CNAO (5% Ce) and MNAO (5% Mn).

Fixed-bed models	Parameters	Adsorbents	
		CNAO	MNAO
Bohart–Adams	kab [mL mg^{-1} min^{-1}]	0.025	0.026
	Nab [mg mL^{-1}]	0.24	0.22
	R^2	0.991	0.991
Clark	rck [1 min^{-1}]	0.33	0.34
	Ack (dimensionless)	457.62	369.11
	R^2	0.991	0.991
Yoon and Nelson	tal [min]	18.50	17.22
	kyn [1 min^{-1}]	0.33	0.34
	R^2	0.991	0.991

through curves of CO_2 adsorption were also analyzed using three different fixed-bed models. The models used were Bohart–Adams, Clark, and Yoon–Nelson. The experimental data were fitted with these models using CAVS software, which considered the operational parameters of the packed column adsorption process, such as the CO_2 inlet concentration, the flow rate, the column dimensions, the adsorbent mass, and the porosity (Figure 3B,C). **Table 2** shows the values of the parameters and the coefficient of determination (R^2) for each model and each adsorbent. According to the results, all the models had a similar R^2 value of 0.991 for both CMNAO and MNAO, indicat-

**ADVANCED
SCIENCE NEWS**

www.advancedsciencenews.com

**ADVANCED
SUSTAINABLE
SYSTEMS**

www.advsustainsys.com

Figure 4. ATR FT-IR of CNAO (5% Ce) and MNAO (5% Mn) after adsorbing CO_2.

Table 3. CO_2 saturation capacities of CNAO and MNAO after regeneration at different temperatures.

Adsorbent	Temperature [°C]	CO_2 saturation capacity [mmol g^{-1}]
CNAO	200	4.69
	300	5.85
	400	12.09
MNAO	200	3.89
	300	5.07
	400	10.12

ing a good fit of models to the experimental results. The maximum amount of CO_2 that could be adsorbed per unit mass of adsorbent (saturation capacity, Nab) of CNAO was higher than that of MNAO, suggesting a higher adsorption capacity for CO_2. The rate of adsorption per unit time of CNAO was also slightly lower than that of MNAO, implying lower adsorption kinetics for CO_2. The dimensionless parameter (a measure of the affinity between the adsorbent and the adsorbate) of the Clark model was higher for CNAO than for MNAO, indicating a stronger affinity for CO_2. The breakthrough time (the time when the outlet percentage of CO_2 reached 50% of the inlet percentage) was longer for CNAO than for MNAO as to the Yoon–Nelson model, reflecting that the adsorbent could saturate more CO_2.

Therefore, it can be concluded that CNAO was a better adsorbent than MNAO for CO_2 capture from flue gas streams because it had a smaller size and larger surface area compared to MNAO, as revealed by multiple characterization techniques such as XRD, HRTEM, and BET, which worked synergistically to create a material with a greater number of accessible adsorption sites. The agreement between experimental data and model fitting further solidifies this observation.

2.4. ATR FT-IR of CO_2 Adsorbed onto CNAO and MNAO

ATR FT-IR spectroscopy was used to explore the CO_2 adsorbed onto CNAO and MNAO. ATR FT-IRS is a technique that uses ATR crystal to measure the IR spectra of thin layers of adsorbed molecules on a solid surface. The IR spectra can provide information about the chemical bonds, functional groups, and molecular vibrations of the adsorbed species.[30]

According to the results from **Figure 4**, the ATR FT-IR spectra of CO_2 adsorbed onto CNAO and MNAO show different features from the un-adsorbed one that indicate the presence of different types of CO_2 species on the surface of our mixed oxides. For both CNAO and MNAO, the spectra show four peaks at 2325, 1600, 1111, and 621 cm^{-1}. As stated in the literature,[31] the peak at 2325
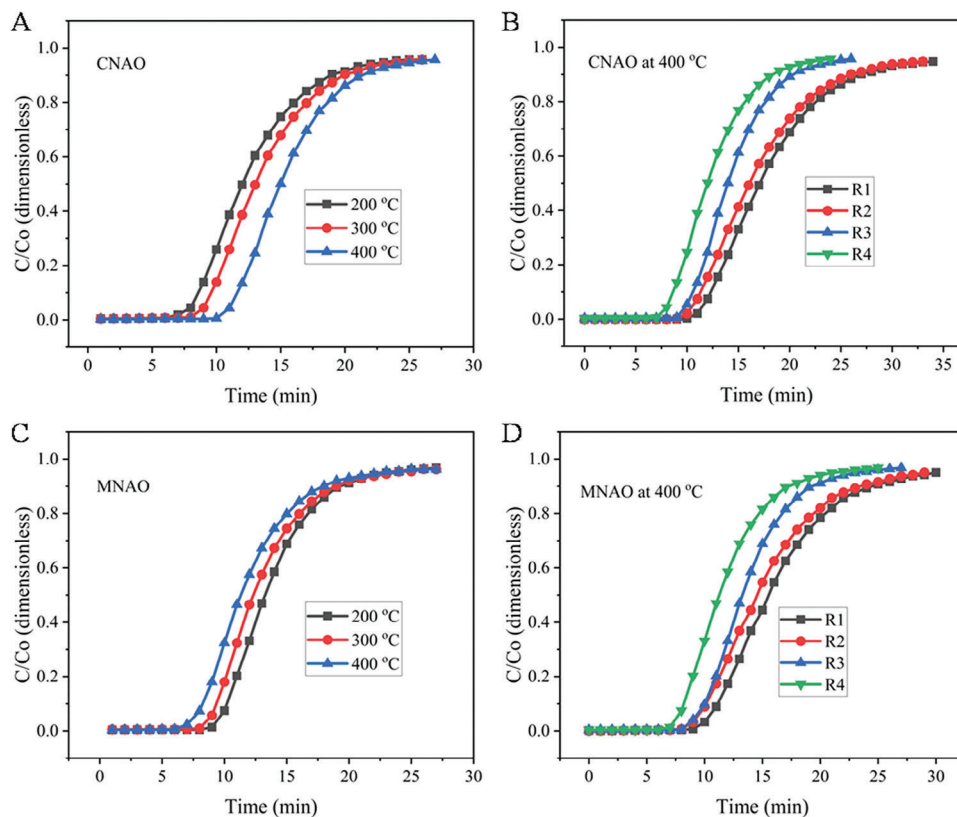
cm^{-1} corresponds to linearly adsorbed CO_2 on the metal sites of the adsorbent, such as Ni, Ce, Mn, or Al. The peak at 1600 cm^{-1} pertains to bidentate carbonate species formed by the reaction of CO_2 with the metal oxides or surface hydroxyl groups of the adsorbent resulting from ambient humidity in the column. The peak at 1111 cm^{-1} is ascribed to mono-dentate carbonate species, which are more stable than bidentate carbonate which can be removed by heating to high temperature. The peak at 621 cm^{-1} is related to bulk carbonate species, which are formed by the diffusion of CO_2 into the lattice of the catalysts where the carbonate is bonded to more than a single metal. The peak at 1111 cm^{-1} is more intense in MNAO, whereas the peak at 621 cm^{-1} is significantly more intense in CNAO.

The presence of these different CO_2 species, indicated by newly appeared peaks in ATR FT-IR spectra taken after the adsorption test, suggests that the mixed metal oxides have a high CO_2 adsorption capacity. The doping of Ce and Mn may enhance CO_2 adsorption by creating more oxygen vacancies and basic sites on the surface of the MMOs at different degrees.[30] Doping MMOs with Ce and Mn introduces foreign cations (Ce^{4+} and Mn^{2+}) into the lattice structure, creating a charge imbalance. To compensate for this imbalance, some lattice oxygens are removed or migrated, forming oxygen vacancies. Due to its higher charge, Ce^{4+} is generally more likely to form oxygen vacancies compared to Mn^{2+} cations. The presence of oxygen vacancies can act as favorable sites for CO_2 adsorption, providing electron density for CO_2 activation. In addition, migrating oxygen ions, when reaching the surface, can act as surface basic sites due to their negative charge, potentially interacting with and attracting CO_2 molecules.[9,16,32]

2.5. Regeneration

2.5.1. Impact of Temperature on Regenerability

The regeneration efficiency of the materials was studied at different temperatures, as presented in **Table 3**, in terms of the impact of regeneration temperature on the CO_2 saturation capacity CNAO and MNAO. The CO_2 saturation capacity of CNAO increased from 4.69 mmol g^{-1} at 200 °C to 12.09 mmol g^{-1} at 400 °C regeneration temperature; while, the CO_2 saturation capacity of MNAO increased from 3.89 mmol g^{-1} at 200 °C to 10.12 mmol g^{-1} at 400 °C regeneration temperature. The results indicated that the saturation capacity of both MMOs increased with regeneration temperature, likely due to the

ADVANCED
SCIENCE NEWS

www.advancedsciencenews.com

ADVANCED
SUSTAINABLE
SYSTEMS

www.advsustainsys.com

Figure 5. A,C) Effect of temperature on regeneration of CO_2-captured NCAO and MNAO and B,D) multiple regeneration performance of CO_2-captured NCAO and MNAO.

higher regeneration temperature removing more surface contaminants and exposing more active sites.[33] This can also be assured from **Figure** 5A,C which indicates that the saturation time decreased with increasing regeneration temperature in both materials.

The CNAO has a higher saturation capacity than MNAO at all regeneration temperatures. This is most likely due to Ce having a higher oxidation state than Mn, which might give it a greater affinity for CO_2.[34] These results suggest that CNAO is a more promising material for capturing and storing CO_2. Based on these findings, the repeated regeneration performances of CNAO and MNAO were studied at 400 °C.

2.5.2. Regeneration Cycle

Table 4 shows the CO_2 saturation capacities of CNAO and MNAO after multiple regeneration cycles at 400 °C. The CO_2 saturation capacity of CNAO decreased from 11.09 to 5.69 mmol g^{-1}; while, that of MNAO decreased from 9.12 to 4.83 mmol g^{-1} after four regeneration cycles. The results indicate that the saturation capacity of both materials decreased with an increasing number of regeneration cycles, likely due to damage caused by the regeneration process, which reduced the number of available adsorption sites.[35] Similarly, Figure 5B,D shows that the saturation time decreased with increasing regeneration cycles in both mixed oxide nanomaterials.

Table 4. CO_2 saturation capacities of CNAO and MNAO after multiple regeneration cycles at 400 °C.

Adsorbent	Regeneration cycle, R	CO_2 saturation capacity [mmol g^{-1}]
CNAO	$R1$	11.09
	$R2$	10.93
	$R3$	7.99
	$R4$	5.69
MNAO	$R1$	9.12
	$R2$	8.96
	$R3$	7.08
	$R4$	4.83

Despite the decrease in saturation capacity, both CNAO and MNAO still exhibited promising CO_2 capture performance, CNAO had a higher saturation capacity than MNAO, and is therefore, a more promising material for large-scale CO_2 capture applications.

It is important to note that the regeneration process is a crucial factor in the long-term performance of CO_2 capture materials. It provides information on the cost of materials effectiveness and sustainability. The regeneration process must be able to remove all of the adsorbed CO_2 without damaging the material.[36] The results of this study suggest that CNAO is more stable than MNAO under multiple regeneration cycles.

Table 5. Comparison of CO_2 adsorption onto CNAO and MNAO with previous studies.

Adsorbents	Experimental conditions				References
	Inlet CO_2 concentration [%]	Temp [°C]	System	CO_2 adsorption capacity [mmol g^{-1}]	
C-700	12.5	30	Purpose-built fixed-bed adsorption	0.676	[42]
Ni–Al–CO_3 DH	15	50	Micromeritics 3Flex	0.87	[43]
Mg_3Al-DOC12-MC	—	300	CO_2-TPD experiments	0.85	[27]
Modified silica capsules	10	75	Packed bed flow reactor	4.45–7.93	[44]
K_2CO_3-promoted Mg–Al LDH/MWNT composite	10	300	Fixed-bed reactor	1.12	[45]
Mg_3Fe_1	10	200	TGA	0.462	[46]
CNT(APTS)	15	50	Packed-bed column	2.45	[47]
Mg–Al–CO_3 hydrotalcite	25	240	TGA	9.27	[48]
Zeolite 13X	20	25	Volumetric	6.9	[49]
Cu-BTC	15	25	Isotherm (IGA)	12.7	[50]
CNAO	13	31	Packed-bed column	11.4	This study
MNAO	13	31	Packed-bed column	10.0	This study

2.6. CO_2 Adsorption Mechanisms

CO_2 adsorption on the synthesized mixed oxides is a surface-mediated process that involves acid–base interactions. The acidic CO_2 molecules react with basic sites on the mixed metal oxides, such as O^{2-} (strong) and metal–O (medium), to form various surface complexes. The complexes can be classified into four categories: linearly adsorbed CO_2, bidentate carbonate, monodentate carbonate, and bulk carbonate. These complexes can be identified by their characteristic peaks in the ATR FT-IR spectra (Figure 4).[27,37,38]

The formation of these complexes depends on the composition and structure of the mixed oxides. The doping of metal ions, such as Ce^{4+} or Mn^{2+}, can create more oxygen vacancies and basic sites on the surface of the mixed oxides, enhancing the CO_2 adsorption potential and stability. The CO_2 adsorption on mixed oxides is reversible and can be regenerated by heating or purging with an inert gas.[27]

The mechanisms of CO_2 adsorption on mixed metal oxides can be explained by the following hypothetical reactions:

i. Linearly adsorbed CO_2: $CO_2 + M–O \rightarrow M–OCO + O$, where M is a metal site such as Ni, Ce, Mn, or Al. This reaction occurs at low temperatures and is reversible by heating or purging with an inert gas.[39]

ii. Bidentate carbonate: $CO_2 + MO \rightarrow M–OOCO$. This is stable up to 240 °C. In addition, $CO_2 + 2OH^- \rightarrow CO_3^{2-} + H_2O$, where OH^- is a surface hydroxyl group, possibly due to some residual water vapor that might be present in the column due to the ambient humidity.[39,40]

iii. Monodentate carbonate: $CO_2 + MO \rightarrow M–O–CO_2$. This is more stable than bidentate carbonate. This can also be expressed as bulk carbonate: $CO_2 + O^{2-} \rightarrow CO_3^{2-}$, where O^{2-} is lattice oxygen. It involves the diffusion of CO_2 into the bulk of the mixed metal oxides in which the carbonate is bonded to

more than one metal. It can be decomposed at a temperature of more than 340 °C.[39-41]

2.7. Comparison With Previous Studies

In Table 5, we compared the CO_2 adsorption capacities of CNAO (11.4 mmol g^{-1}) and MNAO (10.0 mmol g^{-1}) with those reported in previous studies of decades back. Our results show that the CO_2 adsorption capacities of CNAO and MNAO are promising compared to the literature. The CO_2 adsorption capacities reported in the reviewed papers ranged from 0.46 to 9.27 mmol g^{-1}, with the majority falling below 2 mmol g^{-1}.

3. Conclusion

We synthesized two nanomaterials, CNAO and MNAO, from layered double hydroxides and evaluated their CO_2 adsorption performance using a packed-bed column experiment, which closely resembles practical applications at full scale. The materials were characterized by various techniques, and their mechanisms of CO_2 adsorption were also analyzed. We found that CNAO had better CO_2 adsorption capacity and efficiency compared to MNAO due to its higher surface area and stronger CO_2 adsorption affinity.

Our findings suggest that CNAO and MNAO are promising nanomaterials for CO_2 capture applications. They can be easily synthesized using a simple co-precipitation method and calcination. They have high thermal stability, which makes them suitable for long-term use in industrial settings. They can also be modified by different metal dopants to tailor their CO_2 adsorption properties and selectivity. The long-term stability and durability of CNAO and MNAO under repeated adsorption–desorption cycles were investigated. CNAO has a higher saturation capacity after regeneration than MNAO and is therefore a more promising material for large-scale CO_2 capture applications
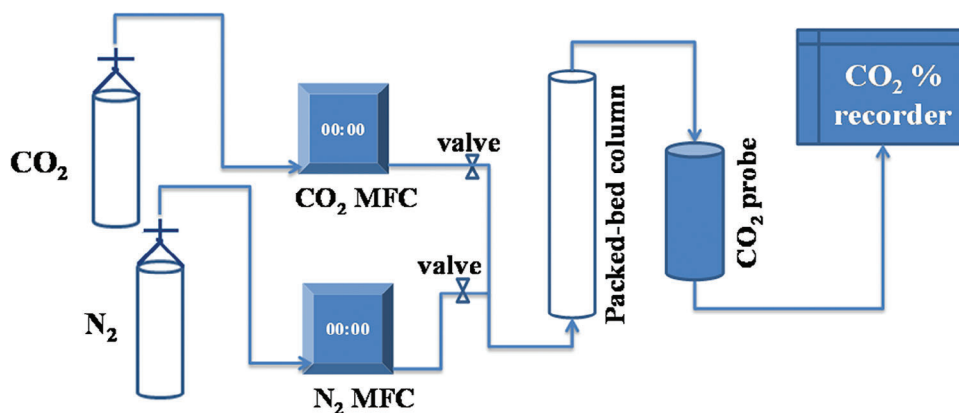
**ADVANCED
SCIENCE NEWS**

www.advancedsciencenews.com

**ADVANCED
SUSTAINABLE
SYSTEMS**

www.advsustainsys.com

Figure 6. A design of in-lab-built packed-bed column experiment for CO_2 adsorption.

The CO_2 adsorption performance of CNAO and MNAO may vary depending on the operating conditions, such as temperature, pressure, gas composition, and flow rate. Therefore, more experiments are needed to optimize these parameters and evaluate the effects of different gas mixtures on the CO_2 adsorption behavior of the materials. These aspects will provide more comprehensive information on the potential of CNAO and MNAO as promising nanomaterials for CO_2 capture applications.

4. Experimental Section

Chemicals and Materials: To synthesize Mn and Ce-doped Ni–Al mixed oxides, several chemicals were used. These included nickel(II) chloride ($NiCl_2.6H_2O$, 97%, from LOBA CHEMIE PVT. LTD), aluminum nitrate ($AlCl_3.6H_2O$, 98%, from CDH(P) Ltd), manganese sulphate ($MnSO_4.H_2O$, 98%, SAMIR Tech-chem PVT. LTD), and ammonium cerium(IV) nitrate ($Ce(NH_4)_2(NO_3)_6$, 0.1 м, from INDETA Chemicals (India) Pvt. Ltd.). Sodium hydroxide (NaOH) and sodium carbonate (Na_2CO_3) were purchased from Merck. These chemicals were of analytical reagent (A.R.) grade. The solutions used in the experiments were prepared using Milli-Q water.

The flue gas mixture (87% N_2 and 13% CO_2) was used as simulated gas for CO_2 capture studies. Aalborg DPC Digital Mass Flow Controllers were used to control the flow of CO_2 inlet and it also indicates the pressure and temperature. A CO_2 meter (VAISALA) with a CO_2 sensor/probe was used to record the online CO_2 concentrations. The Pyrex glass tube of 12 cm in length and 11.19 mm in diameter and inert ceramic balls were used for packing the adsorbents.

Synthesis of the Mixed Oxides: First, the LDH precursors which contained the dopants (Ce to replace 5% of Al and Mn to replace 5% of Ni) were synthesized via the co-precipitation method reported by Wagassa et al. 2023.[51] These LDHs were synthesized under a regulated pH condition of 10. The obtained LDHs were calcined in a microwave furnace at 450 °C for 2 h to produce the corresponding mixed oxides. Finally, NAO, MNAO, and CNAO codes were given to the resulting un-doped, Mn-doped, and Ce-doped mixed oxides, respectively.

Characterization of the Mixed Oxides: A variety of techniques was used to characterize the MMOs. High-resolution transmission electron microscopy (HRTEM) (JEOL JEM 2100 PLUS) instrument was used to study the surface morphology of the mixed oxides. Energy dispersive X-ray spectroscopy (EDS) was used to identify the elemental makeup of the mixed oxides. X-ray photoelectron spectroscopy (XPS) of Omicron ESCA equipment from Oxford Instruments, Germany, was used to examine the oxidation states of elements in the surface layer of the mixed oxides. X-ray powder diffraction (XRD) patterns were produced using a Rigaku Miniflex-600 X-ray diffractometer with a Cu Kα source, scanning at a constant rate

over a two range of 10–90°. Over a 400 to 4000 cm^{-1} range, attenuated total reflection Fourier transform infrared (ATR FT-IR) spectroscopy was used to study the functional groups present on the surface of the MMOs using a VERTEX70 spectrometer from BRUKER, Germany. The specific surface area (SSA) and porosity of the synthesized mixed oxides were measured after they were exposed to N_2 gas at 77 K, and the amount of gas adsorbed and desorbed was recorded. The data was then analyzed using the Brunauer–Emmett–Teller (BET) isotherm model with Quantacrome Instruments version 11.0.

CO_2 Adsorption Experimental Setup and Measurements: CO_2 adsorption was studied in a packed-bed column reactor (**Figure 6**). The setup included a mass flow controller (0–500 mL min^{-1}) with pressure and temperature indicators, a Pyrex glass tube (11.19 mm diameter, 12 cm length), an online CO_2 meter (0–20 vol%, 0.1% accuracy), and all necessary valves and connections.

To investigate the adsorption of CO_2 on mixed oxides, ≈100 mg of the material was placed in a column with inert ceramic balls. The ceramic balls were thoroughly pre-treated by washing them with de-ionized water and heating them at 150 °C for 4 h before use. A gas mixture containing 13% ± 1 vol% CO_2 was passed through the column at a flow rate of 20 mL min^{-1}, inlet pressure of 14.15 ± 0.1 psi, temperature of 31 °C ± 2 °C, and bed height of 10 cm. Blank experiments were conducted by running the column packing using ceramic balls only.

To ensure isothermal conditions for the sorbet particles, the column was flushed with N_2 gas before each CO_2 adsorption experiment to eliminate any previously present gas. A CO_2 analyzer was used to measure and record the outflow CO_2 amount. The outflow data were collected until the concentration of outflow was greater than 90% of the concentration of CO_2 inlet. This steady state condition was evident from the graph of CO_2 out versus time displayed on the CO_2 analyzer. The collected data were then utilized to investigate the breakthrough curve and estimate the adsorption capacity of the adsorbents.

It should be noted that the adsorbent's pressure loss was modest due to its low superficial velocity and bed height was few. Thus, the flow rates at the inlet and exit of the column were presumed to be equal for each experimental condition, and the pressure across the bed remained constant. The breakthrough (q_b, at 10%), saturation (q_s, at 90%), and equilibrium (q_e, at 100%) capacities of the synthesized MMOs were determined using CO_2 mass balancing Equation (2) with necessary conversions.[52,53]

$$q = \frac{Q}{m \times 22.4} \int_0^t (C_i - C_e)dt \tag{2}$$

where q denotes the CO_2 adsorption capacity in mol g^{-1}, Q flow rate of gas in L min^{-1}, m mass of adsorbent in g, and t time in min. C_i and C_e were intake and effluent CO_2 amounts (percentage of volume).

**ADVANCED
SCIENCE NEWS**

www.advancedsciencenews.com

**ADVANCED
SUSTAINABLE
SYSTEMS**

www.advsustainsys.com

Fixed-Bed Adsorption Models: The Bohart–Adams, Clark, and Yoon–Nelson models are mathematical models that can be used to predict the breakthrough curve of a packed column adsorption process. The breakthrough curve is a plot of the effluent concentration of the adsorbate versus the time or volume of the effluent. The models are based on different assumptions and have different forms of equations.

The Bohart–Adams model assumes that the rate of adsorption is proportional to the remaining adsorption capacity of the adsorbent and the concentration of the adsorbate in the liquid phase. The model also neglects the mass transfer resistance and axial dispersion in the column. The model can be expressed as:[54]

$$\ln\left(\frac{C}{C_0}\right) = -k_{BA}N_0\left(1 - e^{-k_{BA}t}\right) + k_{BA}C_0 t \tag{3}$$

where C is effluent concentration, C_0 is initial concentration, k_{BA} is Bohart–Adams rate constant, N_0 is initial adsorption capacity of the adsorbent, and t is time.

The Clark model describes the rate of adsorption as a function of the driving force, which is the difference between the equilibrium concentration and the actual concentration of the adsorbate on the adsorbent. The model also considers the mass transfer resistance and the axial dispersion in the column. It can be expressed by Equation (4):[55]

$$\frac{dC}{dt} = -\frac{k_C A}{V_L}(C_e - C) + D_L \frac{d^2 C}{dz^2} \tag{4}$$

where k_C is the Clark rate constant, A is cross-sectional area of the column, V_L is the volume of liquid in the column, C_e is an equilibrium concentration, D_L is the axial dispersion coefficient, and z is the axial distance.

The Yoon–Nelson model assumes that the rate of adsorption is directly related to the probability of adsorption, which decreases linearly with time. The model also neglects mass transfer resistance and axial dispersion in the column. It can be expressed by Equation (5):[54]

$$\ln\left(\frac{C}{C_0 - C}\right) = -k_{YN}t + \tau \tag{5}$$

where k_{YN} is the rate constant and τ is the time required for a 50% breakthrough.

These models can be used to fit experimental data and estimate parameters of the models using linear or nonlinear regression methods. The models can also be used to predict the breakthrough time, adsorption capacity, and mass transfer coefficients of a fixed-bed adsorption process. Therefore, it is important to choose a suitable model for a specific system and validate it with experimental data.

Supporting Information

Supporting Information is available from the Wiley Online Library or from the author.

Acknowledgements

Conflict of Interest

The authors declare no conflict of interest.

Data Availability Statement

The data that support the findings of this study are available from the corresponding author upon reasonable request.

Keywords

[1] S. Sharma, F. Maréchal, *Front. Energy Res.* **2019**, *7*, 143.
[2] F. O. Ochedi, J. Yu, H. Yu, Y. Liu, A. Hussain, *Environ. Chem. Lett.* **2021**, *19*, 77.
[3] H. Zeng, X. Qu, D. Xu, Y. Luo, *Front. Chem.* **2022**, *10*, 939701.
[4] G. Manohara, M. M. Maroto-Valer, S. Garcia, *Dalton Trans.* **2020**, *49*, 923.
[5] G. Manohara, D. Norris, M. M. Maroto-Valer, S. Garcia, *Dalton Trans.* **2021**, *50*, 7474.
[6] A. Lund, G. Manohara, A.-Y. Song, K. M. Jablonka, C. P. Ireland, L. A. Cheah, B. Smit, S. Garcia, J. A. Reimer, *Chem. Mater.* **2022**, *34*, 3893.
[7] F. Li, X. Duan, in *Layered Double Hydroxides* (Eds: X. Duan, D. G. Evans), Springer, Berlin **2006**, pp. 193–223.
[8] L. K. G. Bhatta, U. M. Bhatta, K. Venkatesh, *Sustainable Agric. Rev.* **2019**, *38*, 63.
[9] S. I. Garcés-Polo, J. Villarroel-Rocha, K. Sapag, S. A. Korili, A. Gil, *Chem. Eng. J.* **2018**, *332*, 24.
[10] S. Li, X. Zhu, D. Wang, P. Hao, F. Zhou, Y. Shi, R. Wang, N. Cai, *Chem* **2023**, *5*, 100113.
[11] A. N. Wagassa, A. Bansiwal, T. A. Shifa, E. A. Zereffa, *RSC Adv.* **2024**, *14*, 1229.
[12] D. Iruretagoyena Ferrer, *Supported Layered Double Hydroxides as CO$_2$ Adsorbents for Sorption-Enhanced H$_2$ Production*, Springer, Cham, Switzerland **2016**, p. 141.
[13] M. K. A. Mesfer, M. Danish, M. I. Khan, I. H. Ali, M. Hasan, A. E. Jery, *Processes* **2020**, *8*, 1233.
[14] C. Megías-Sayago, R. Bingre, L. Huang, G. Lutzweiler, Q. Wang, B. Louis, *Front. Chem.* **2019**, *7*, 551.
[15] I. Iliuta, M. C. Iliuta, *Ind. Eng. Chem. Res.* **2015**, *54*, 12455.
[16] X. Zhu, T. Ge, F. Yang, M. Lyu, C. Chen, D. O'Hare, R. Wang, *J. Mater. Chem. A* **2020**, *8*, 16421.
[17] A. Adamu, F. Russo-Abegão, K. Boodhoo, *BMC Chem. Eng.* **2020**, *2*, 2.
[18] Z. Lv, S. Yang, H. Zhu, L. Chen, N. S. Alharbi, M. Wakeel, A. Wahid, C. Chen, *Appl. Surf. Sci.* **2018**, *448*, 599.
[19] B. Ali, B. Naceur, E. Abdelkader, E. Karima, B. Nourredine, *Int. J. Environ. Anal. Chem.* **2020**, *102*, 3207.
[20] S. K. Chatterjee, *PHI Learning Pvt. Ltd.* **2010**.
[21] Á. G. Aponte, M. A. L. Ramírez, Y. C. Mora, J. F. Santa Marín, R. B. Sierra, *AIMS Mater. Sci.* **2020**, *7*, 468.
[22] G. Srikesh, A. S. Nesaraj, *J. Asian Ceram. Soc.* **2020**, *8*, 835.
[23] Z. Gao, J. Liang, J. Yao, Q. Meng, G. He, H. Chen, *J. Environ. Chem. Eng.* **2021**, *9*, 105405.
[24] S. Wang, H. Liu, Z. Li, J. Zhu, *J. Mater. Sci.: Mater. Electron.* **2019**, *30*, 7524.
[25] X. Wang, X. Hou, Q. Wang, W. Ge, S. Guo, *J. Solid State Electrochem.* **2019**, *23*, 1121.
[26] Y. Zhao, S. Cao, L. Zeng, M. Xia, N. Jakse, J. Li, *Metall. Mater. Trans. A* **2023**, *54*, 646.
[27] B. Wang, X. Zhang, Y. Liu, D. Li, Y. Lin, *Chem. Eng. J.* **2022**, *446*, 136842.
[28] Y. Xu, B. Xiao, Y. Feng, W. Yang, Y. Lv, *J. Nat. Gas Sci. Eng.* **2021**, *94*, 104029.
[29] M. Zhang, J. Zhang, Z. Zhou, S. Chen, T. Zhang, F. Song, Q. Zhang, N. Tsubaki, Y. Tan, Y. Han, *Appl. Catal., B* **2020**, *264*, 118522.

**ADVANCED
SCIENCE NEWS**

www.advancedsciencenews.com

**ADVANCED
SUSTAINABLE
SYSTEMS**

www.advsustainsys.com

[30] I. A. Mudunkotuwa, A. Al Minshid, V. H. Grassian, *Analyst* **2014**, *139*, 870.

[31] J. Hammerli, J. Hermann, P. Tollan, F. Naab, *Contrib. Mineral. Petrol.* **2021**, *176*, 105.

[32] M. A. A. Aziz, A. A. Jalil, S. Wongsakulphasatch, D.-V. N. Vo, *Catal. Sci. Technol.* **2020**, *10*, 35.

[33] J. Hack, N. Maeda, D. M. Meier, *ACS Omega* **2022**, *7*, 39520.

[34] C. A. Trickett, A. Helal, B. A. Al-Maythalony, Z. H. Yamani, K. E. Cordova, O. M. Yaghi, *Nat. Rev. Mater.* **2017**, *2*, 17045.

[35] S. Bustillos, A. Alturki, D. Prentice, E. C. La Plante, M. Rogers, M. Keller, R. Ragipani, B. Wang, G. Sant, D. A. Simonetti, *Front. Energy Res.* **2020**, *8*, 610392.

[36] A. Kurlov, A. M. Kierzkowska, T. Huthwelker, P. M. Abdala, C. R. Müller, *Phys. Chem. Chem. Phys.* **2020**, *22*, 24697.

[37] Y. Gao, Z. Zhang, J. Wu, X. Yi, A. Zheng, A. Umar, D. O'Hare, Q. Wang, *J. Mater. Chem. A* **2013**, *1*, 12782.

[38] L. Smoláková, K. Frolich, I. Troppová, P. Kutálek, E. Kroft, L. Čapek, *J. Therm. Anal. Calorim.* **2017**, *127*, 1921.

[39] S. Kumar, S. K. Saxena, *Mater. Renew. Sustain. Energy* **2014**, *3*, 1.

[40] K. Yoshikawa, H. Sato, M. Kaneeda, J. N. Kondo, *J. CO2 Util.* **2014**, *8*, 34.

[41] Y. Lwin, F. Abdullah, *J. Therm. Anal. Calorim.* **2009**, *97*, 885.

[42] C. Goel, H. Bhunia, P. K. Bajpai, *J. Environ. Chem. Eng.* **2016**, *4*, 346.

[43] S. Shang, A. Hanif, M. Sun, Y. Tian, Y. S. Ok, K. Iris, D. C. Tsang, Q. Gu, J. Shang, *J. Hazard. Mater.* **2019**, *373*, 285.

[44] G. Qi, Y. Wang, L. Estevez, X. Duan, N. Anako, A.-H. A. Park, W. Li, C. W. Jones, E. P. Giannelis, *Energy Environ. Sci.* **2011**, *4*, 444.

[45] L. K. G. Bhatta, S. Subramanyam, M. D. Chengala, U. M. Bhatta, P. Guha, R. P. H. Dinakar, K. Venkatesh, *Energy Fuels* **2016**, *30*, 4244.

[46] Q. Wang, H. H. Tay, D. J. W. Ng, L. Chen, Y. Liu, J. Chang, Z. Zhong, J. Luo, A. Borgna, *ChemSusChem* **2010**, *3*, 965.

[47] F. Su, C. Lu, H.-S. Chen, *Langmuir* **2011**, *27*, 8090.

[48] S. Kim, S. G. Jeon, K. B. Lee, *ACS Appl. Mater. Interfaces* **2016**, *8*, 5763.

[49] V. Garshasbi, M. Jahangiri, M. Anbia, *Appl. Surf. Sci.* **2017**, *393*, 225.

[50] Z. Liang, M. Marshall, A. L. Chaffee, *Energy Fuels* **2009**, *23*, 2785.

[51] A. N. Wagassa, L. T. Tufa, J. Lee, E. A. Zereffa, T. A. Shifa, *Global Chall.* **2023**, *7*, 2300018.

[52] L. Li, X. Wen, X. Fu, F. Wang, N. Zhao, F. Xiao, W. Wei, Y. Sun, *Energy Fuels* **2010**, *24*, 5773.

[53] M. Amiri, S. Shahhosseini, A. Ghaemi, *Energy Fuels* **2017**, *31*, 5286.

[54] O. B. Omitola, M. N. Abonyi, K. G. Akpomie, F. A. Dawodu, *Appl. Water Sci.* **2022**, *12*, 94.

[55] S. Biswas, U. Mishra, *J. Chem.* **2015**, *2015*, 1.